






Shelving and latching spin readout in atom qubits in silicon

Edyta N. Osika ^{1,2} Samuel K. Gorman,^{2,3} Serajum Monir,^{1,2} Yu-Ling Hsueh ^{1,2} Marcus Borszcz ¹ Helen Geng,^{2,3} Brandur Thorgrimsson ^{2,3} Michelle Y. Simmons,^{2,3} and Rajib Rahman ^{1,2}

¹*School of Physics, University of New South Wales, Sydney, NSW 2052, Australia*

²*Silicon Quantum Computing Pty Ltd., Level 2, Newton Building, University of New South Wales, Sydney, Kensington NSW 2052, Australia*

³*The Centre of Excellence for Quantum Computation and Communication Technology, School of Physics, University of New South Wales, Sydney, NSW 2052, Australia*



(Received 5 April 2022; revised 8 July 2022; accepted 15 July 2022; published 22 August 2022)

Singlet-triplet qubits typically require large magnetic field gradients on the order of militeslas to achieve high-fidelity electrically-controlled qubit operations. However, such large magnetic field gradients in quantum dot systems also increase charge noise and provide a relaxation pathway from the triplet to singlet qubit state, making high-fidelity readout challenging. Recently, shelving and latched readout have been employed in gate-defined quantum dots and donor-dot systems to achieve readout fidelities of 80% and 99.86%, respectively. In this paper, we theoretically examine shelving and latched singlet-triplet readout techniques for multidonor-based qubits in silicon where the large phosphorus hyperfine interaction of the order of 100 MHz gives rise to large effective magnetic field gradients (equivalent to tens of mT) but where it can change in time due to the presence of nuclear spin flips. Using numerical simulations, we show that shelving readout does not work giving a zero average visibility for multidonor quantum dots, due to the time-varying nuclear spin polarization. To remedy this we propose adding a calibration step, in which we derive the nuclear spin polarization from a single shelving readout of a singlet state, before every qubit operation. The derived information can then be used via a feed-forward protocol to apply correct readout mapping, greatly improving the overall readout fidelity to >99%. We also simulate the latched readout mechanism, which is resistant to nuclear polarization changes and is thus promising for achieving high visibility readout. Here we observe a nonzero readout visibility irrespective of the nuclear spin flipping. Finally, we discuss how to optimize the readout visibility in the presence of strong hyperfine interactions and show that for both readout methods we can obtain readout fidelity >99%. These results demonstrate that singlet-triplet qubits based on multidonor quantum dots are a promising route for future electrically controlled qubits in silicon.

DOI: [10.1103/PhysRevB.106.075418](https://doi.org/10.1103/PhysRevB.106.075418)

I. INTRODUCTION

Spin qubits based on phosphorus donors in silicon [1] have demonstrated excellent coherence and relaxation times [2,3]. Those long coherence times, together with atomistic fabrication technologies based on scanning tunneling microscopy (STM) [4], make donor qubits a promising semiconductor platform for scalable quantum information processing. While the implementation of magnetic control of single electron qubits in Si:P is well established [5,6], there is still high interest in alternative qubit systems, which can be controlled by purely electrical means simplifying the task of scaling up quantum computers [7,8]. One of the proposals of an electrically-controlled system is the singlet-triplet qubit [9–11] comprised of two electrons localized within a double quantum dot (QD) and coupled by the exchange interaction. Multiple realizations of singlet-triplet qubits have been implemented in double QD [10,12–15] and quantum dot-donor systems [16]. Crucially, for large-scale implementations, singlet-triplet qubits can be measured dispersively via a single gate [17]. This dispersive readout allows for minimal gate densities [18] and the possibility for frequency-multiplexed qubit measurements [19] extremely useful for large quantum systems.

To realize purely electrical control of the singlet-triplet qubit, the two quantum dots of the system need to be characterized by different spin Zeeman splittings. The Zeeman energy difference ΔE_z allows coupling between the singlet and triplet states and therefore the ability to perform qubit rotations. In electrostatically-defined quantum dots ΔE_z can be produced by a surrounding nuclear spin bath [10,12], a micromagnet [15] or a difference in g factors in the two quantum dots [20,21]. In donor-based devices the same coupling can be achieved using the hyperfine interaction between the electron and nuclear spins inherently present in the system. The electron-nuclear hyperfine interaction can be described as an effective magnetic field experienced by the electrons. This field is homogeneous if the hyperfine interaction is the same for both dots, or treated as a magnetic field gradient causing a difference in the Zeeman splitting ΔE_z if the interaction differs between the dots. Although large ΔE_z is desirable as it is necessary for fast singlet-triplet qubit operation, it is also a source of fast triplet relaxation. This fast relaxation [11] is most prominent in context of singlet-triplet qubit readout, significantly limiting the visibility of the standard Pauli spin-blockade readout (PSBR). Additionally, in donor-based devices ΔE_z can change with time as nuclear spins can undergo

uncontrolled flips [22]. These additional processes need to be accounted for when designing and interpreting readout outcomes for singlet-triplet qubit in donor-based devices.

Pauli spin-blockade readout is one of the most standard and widely-used singlet-triplet readout techniques [23,24]. In PSBR the system is pulsed from the (1,1) charge region to the Pauli-blocked (0,2) charge configuration region [where (n_L, n_R) corresponds to n_L electrons in left and n_R in right dot]. There, the singlet state is mapped to the (0,2) charge configuration while the triplet state stays blocked in (1,1) due to the high single-dot exchange energy making the triplet (0,2) state inaccessible. This method has a relatively small contrast in the signal between singlet and triplet states and suffers from fast triplet relaxation when singlet-triplet mixing is present in the system. Alternative singlet-triplet readout methods have been developed [16,25–32] to address the shortcomings of PSBR and adjust the readout process to the needs of specific quantum dot architectures. The improved visibility of the new readout methods proposed, as compared to PSBR, is achieved via either mapping the triplet to some metastable state, which minimizes relaxation, or mapping the (1,1) and (0,2) charge configurations to states with different total number of electrons in the system, which increases signal contrast. Those improvements are especially important in cases when the system is subject to large magnetic field gradients [31] or when distinguishing (1,1) and (0,2) charge configurations is challenging [28].

In this paper, we focus on two types of singlet-triplet readout methods, which have proven to give considerable advantages as compared to PSBR. The first is shelving readout, recently demonstrated in GaAs gate-defined quantum dots [31], which performs best for systems subject to high magnetic field gradients. Although this method gives similar signal contrast to Pauli blockade readout, as it measures (1,1) and (0,2) charge configurations, it minimizes the triplet to singlet relaxation by mapping one of electron spin configurations $|\uparrow\downarrow\rangle$ or $|\downarrow\uparrow\rangle$ to a metastable, spin-polarized triplet state. The second technique, latched readout, demonstrated in dot-donor system [30], increases the contrast between singlet and triplet states by mapping them to charge configurations differing by one electron, i.e., (0,2) and (1,2). We discuss the applicability of both those methods for multidonor qubits, where we show the impact of the nuclear spin flips present and how to optimize for these. We find that the standard shelving method gives near zero visibility due to the averaging over different possible ΔE_z values that occur due to the time-dependent nuclear spin configurations. We show this can be improved by adding a calibration step before each qubit operation. The calibration step performs a single shelving readout protocol on a prepared initial singlet state, from which information about the current nuclear spin polarization can be extracted. This information is used to map the readout correctly in the following qubit operation, which leads to an improvement of readout fidelity to $>99\%$. We find that latched readout works better for donor qubits, as it is insensitive to the sign of ΔE_z . However, in latched readout we have to take care to design the tunneling rates and timescales of the process, since these are sensitive to the specific atomistic arrangement of donors within the device and need to be carefully optimized for a given arrangement. We discuss the optimization procedure

in detail, indicating what kind of requirements need to be fulfilled to reach a readout fidelity of $>99\%$.

II. MODEL

We consider two quantum dots of phosphorus donors in silicon—see Fig. 1(a), each dot consisting of at least one P donor (red arrows) and occupied by a single electron (black arrows). The two dots are tunnel-coupled allowing the electrons to form singlet and triplet states across both quantum dots. In general each dot can be occupied by any odd number of electrons, in such cases only the behavior of the outer unpaired, highest-energy electron in each dot are investigated. The single electron transistor (SET) serves as an electron reservoir for the donor dots and is used for the readout. The surrounding gates (G_L, G_M, G_R) control the electrostatic environment of the QDs.

Both shelving and latched readout—or more precisely the reverse enhanced version of the latched readout [30]—operate in the charge occupation subspace comprising (1,1), (0,2), and (1,2) configurations—see Fig. 1(b). The electron distribution between the dots is controlled with detuning ϵ , while loading of additional electrons from the SET is determined with a parameter γ , which represents a global energy shift of both QDs. Both ϵ and γ can be controlled by the control gates surrounding the double-dot system.

We simulate the readout protocols calculating the two dot system subject to the γ pulses, using an extended version of the model presented in Ref. [31] (see Appendix). The basis for time-dependent calculations spans over the seven system eigenstates, schematically depicted in Fig. 1(c): two (1,2) states, i.e., the $\downarrow S$ and $\uparrow S$, singlet $S(0, 2)$ and four (1,1) states, i.e., the spin-polarized T_- and T_+ and the nonspin-polarized G (ground) and E (excited) state. In the absence of a magnetic field gradient, $\Delta E_z = 0$, the states G and E are split by the exchange interaction J and form singlet $S(1, 1)$ and triplet $T_0(1, 1)$ states, respectively. ΔE_z mixes singlet and triplet states and in the limit of $\Delta E_z \gg J$ it sets $|G\rangle = |\uparrow\downarrow\rangle$ and $|E\rangle = |\downarrow\uparrow\rangle$ (or the opposite for $\Delta E_z < 0$). In the intermediate regime, where J and ΔE_z are comparable, the mixing of S and T_0 (or $\downarrow\uparrow$ and $\uparrow\downarrow$) strongly depends on the relative amplitudes of exchange J and ΔE_z . As the exchange J is controllable with the detuning ϵ between the $S(1, 1)$ - $S(0, 2)$ states, the singlet-triplet mixing can be modulated with ϵ . This effect is shown symbolically with the Bloch spheres at the bottom of Fig. 1(c)—close to $\epsilon = 0$ where $J \gg |\Delta E_z|$, the qubit eigenstates align approximately with the $S - T_0$ axis and for higher detuning where $J \ll |\Delta E_z|$, they align closely with the $\downarrow\uparrow - \uparrow\downarrow$ axis. The transition rates between (1,2) and (1,1)/(0,2) states are calculated using the Fermi golden rule, with Γ_L and Γ_R specifying tunneling rate between SET and left and right QD, respectively (more details in the Appendix).

III. SHELIVING

A. Shelved readout protocol

We first discuss the shelving readout method [31], which is particularly useful for systems with large magnetic field gradients ΔE_z as it maps $|\uparrow\downarrow\rangle$ and $|\downarrow\uparrow\rangle$ states to different charge configurations—(0,2) and (1,1). The

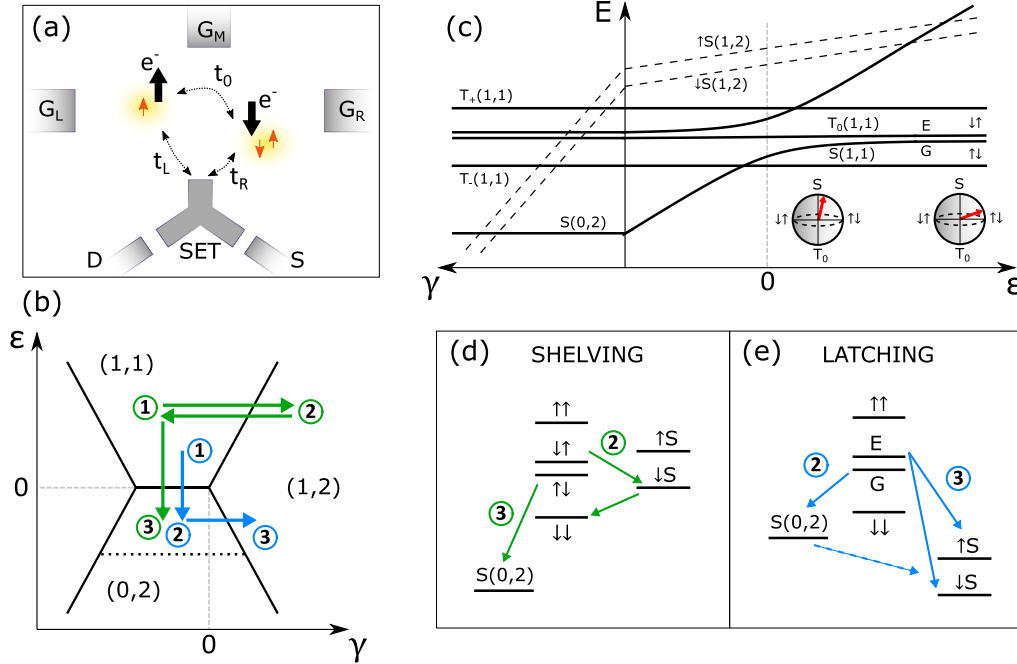


FIG. 1. A comparison of shelving and latched readout in multidonor-based qubits. (a) A schematic of the modelled system: two donor-based quantum dots (left 1P, right 2P), surrounded by G_L , G_M , G_R gates and tunnel-coupled to a SET, each dot occupied by a single electron. Nuclear (electron) spins are represented by orange (black) arrows. t_0 and t_L (t_R) are tunneling between the dots and between left (right) dot and SET, respectively. (b) A charge stability diagram with respect to the detuning between the dots, ϵ with the γ parameter controlling the total number of electrons in the system. Green (blue) arrows represent shelving (latching) readout protocols, with numbers indicating the order of readout steps. The dashed line shows the end of Pauli-blocked region. (c) Schematic representation of the energy levels of (1,2), (0,2), and (1,1) states as a function of γ (left part of the plot) and ϵ (right). [(d),(e)] Scheme of the shelving and latching readout procedure, with the relevant state ladders and transitions indicated by arrows with the numbers corresponding to plot (b).

procedure is schematically shown in Figs. 1(b) (green arrows) and 1(d).

The protocol starts in the (1,1) charge configuration region, preferably at high detuning ϵ , where exchange is negligible and ΔE_z sets the eigenstates to approximately $|G\rangle = |\uparrow\downarrow\rangle$ and $|E\rangle = |\downarrow\uparrow\rangle$. We ramp nonadiabatically along the γ axis in a time t_{in} to γ_{max} in the (1,2) region, and we stay there for a time t_{wait} to allow an electron to tunnel between SET and the dots. If we set γ_{max} so that the $|\downarrow S\rangle$ energy level lies between the $|\downarrow\uparrow\rangle$ and $|\downarrow\downarrow\rangle$ states [see Fig. 1(d)], the subsequent transition $|\downarrow\uparrow\rangle \rightarrow |\downarrow S\rangle \rightarrow |\downarrow\downarrow\rangle$ becomes available, mapping the $|\downarrow\uparrow\rangle$ state to a metastable triplet $|T_- \rangle$. The transition takes place due to electron \downarrow tunneling from the SET to the right dot and then electron \uparrow tunneling back to the SET. At the same time, the $|\uparrow\downarrow\rangle$ energy level does not undergo any transition as the $|\uparrow S\rangle$ state is energetically inaccessible and no electron can tunnel from the SET to the right dot. Next, the system is brought back to point 1 in the (1,1) region and then, by an adiabatic change of detuning, to point 3 in the Pauli-blocked (0,2) region. As a result of this process the ground qubit state $|G\rangle \approx |\uparrow\downarrow\rangle$ maps to the singlet (0,2) state while the excited state $|E\rangle \approx |\downarrow\uparrow\rangle$ maps to the blocked triplet $|T_- \rangle$ of charge configuration (1,1).

The shelved readout method solves the problem of fast $|T_0\rangle \rightarrow |S(0,2)\rangle$ relaxation, which limits the PSBR fidelity. Due to the long relaxation time of the $|T_- \rangle$ state compared to $|T_0\rangle$ [33], the different (0,2) and (1,1) charge configurations can now be measured with better visibilities compared to

the standard PSBR method. Also, the shelving process alone does not introduce any additional relaxation channels as the operation takes place in (1,1)-(1,2) region where the singlet (0,2) is energetically inaccessible. The mapping we obtain via the shelving procedure can also be conveniently used with dispersive readout [17], using just a single gate thus minimizing the device complexity.

In practice, even for large detuning ϵ , the $|\downarrow\downarrow\rangle$ and $|\uparrow\uparrow\rangle$ states are mixed due to the nonzero exchange J . The admixtures of the opposite states can cause leakage, lowering the total readout visibility. Previous experiments performed with gate-defined quantum dots showed shelving readout fidelity of approximately 80% [31]. In the next section we discuss in detail the shelving readout visibility for realistic donor-based devices and show how it can be maximized.

B. Simulations of shelved readout

Here we perform numerical simulations of shelving readout in order to estimate the maximum readout visibility achievable in donor-based qubits. We investigate how the operation parameters of the protocol influence the final singlet-triplet visibility and describe how the varying nuclear spin polarization affects the readout results.

In Fig. 2(a) we present the energy spectra of the system as a function of γ' where $\gamma' = \gamma - \epsilon/2$. The parameter γ' is introduced to describe the QDs energy shift with respect to the (1,1)-(1,2) transition, i.e., for every ϵ we have $\gamma' = 0$ exactly

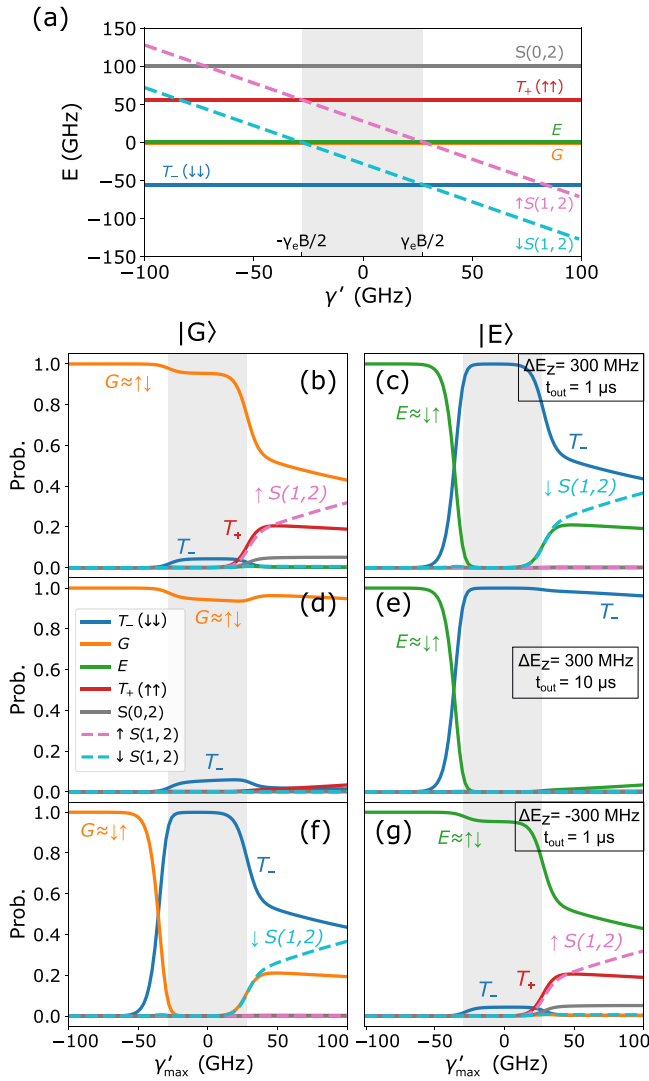


FIG. 2. Simulation of the shelved readout protocol. (a) System energy levels as a function of $\gamma' = \gamma - \epsilon/2$ for $\epsilon = 100$ GHz. Here, the ground $|G\rangle$ and excited $|E\rangle$ qubit states nearly overlap within the energy scale adapted. For $\Delta E_z > 0$ the $|G\rangle$ and $|E\rangle$ states can be described approximately as $\uparrow\downarrow$ and $\downarrow\uparrow$, respectively [as identified in the scheme of Fig. 1(d)]. [(b)–(g)] Final eigenstates probability of shelving $(1) \rightarrow (2) \rightarrow (1)$ process [see Fig. 1(b)] as a function of γ'_{\max} , i.e., the maximal value of γ' that the system is brought to during the shelving [green point (2) in Fig. 1(b)]. Simulations of [(b),(d),(f)] and [(c),(e),(g)] start from initial state set to $|G\rangle$ and $|E\rangle$, respectively. Plots [(b),(c)] show results for $\Delta E_z = 300$ MHz and $t_{\text{out}} = 1 \mu\text{s}$, plots [(d),(e)] present simulations for longer t_{out} time of $10 \mu\text{s}$ and [(f),(g)] of a Zeeman energy difference of the opposite sign $\Delta E_z = -300$ MHz. The shaded region in all the plots indicates the $-\gamma_e B/2 < \gamma' < \gamma_e B/2$ regime, where the shelving readout is the most efficient.

at the (1,1)-(1,2) transition line. Here we use detuning $\epsilon = 100$ GHz—far enough in (1,1) region so that the $S(0,2)$ state lies above all (1,1) levels. We simulate the $(1) \rightarrow (2) \rightarrow (1)$ process of shelving readout [see Fig. 1(b)] in the following way: (i) we start at $\gamma'_{\min} = -100$ GHz, (ii) we increase γ' up to γ'_{\max} value within a t_{in} time, (iii) we stay at the γ'_{\max} point for a t_{wait} time and, (iv) we decrease γ' back to -100 GHz within

t_{out} . In Figs. 2(b)–2(g) we present the final probability of each of the system eigenstates as a function of γ'_{\max} . Thus, each point on those plots represent full $(1) \rightarrow (2) \rightarrow (1)$ shelving simulation [with point (2) specified by γ'_{\max}] and only final probabilities are plotted. Plots [(b),(d),(f)] and [(c),(e),(g)] correspond to simulations starting from the ground $|G\rangle$ and excited $|E\rangle$ state of the singlet-triplet qubit, respectively. We use $\Gamma_L = \Gamma_R = 10^6 \text{s}^{-1}$, however the exact value of Γ_L does not play a significant role in the simulation as the (1,1)-(1,2) tunneling affects only the right dot. We set $t_{\text{in}} = 100$ ns and $t_{\text{wait}} = 10 \mu\text{s}$ —much longer than tunneling time $1/\Gamma_R$. All of these values are experimentally realistic [34]. The detuning $\epsilon = 100$ GHz used in the simulations is equivalent to the exchange interaction $J \approx 40$ MHz (calculated as the energy difference between $|E\rangle$ and $|G\rangle$ states for $\Delta E_z = 0$). The parameters, which we vary in Figs. 2(b)–2(g) are the Zeeman energy difference ΔE_z and shelving-out time t_{out} .

In Figs. 2(b) and 2(c) we show simulations for $\Delta E_z = 300$ MHz (realistic in multidonor quantum dots) and $t_{\text{out}} = 1 \mu\text{s}$. Here, as ΔE_z is several times larger than the exchange interaction, the $|G\rangle$ and $|E\rangle$ states exist predominantly in $|\uparrow\downarrow\rangle$ and $|\downarrow\uparrow\rangle$ spin configurations, respectively. The admixtures of different basis states ($\downarrow\uparrow$ in $|G\rangle$ and $\uparrow\downarrow$ in $|E\rangle$) are of about $(1 - \Delta E_z / \sqrt{\Delta E_z^2 + J^2})/2 \approx 0.004$. We can distinguish three different regions within γ'_{\max} range, in which we can observe distinct outcomes of shelving readout.

(i) First, we can see that in $\gamma'_{\max} \ll 0$ region, we do not observe any tunneling irrespective of what is the initial qubit state. That is reflected by the constant ≈ 1 probability of $|G\rangle$ and $|E\rangle$ states on the left sides of Figs. 2(b) and 2(c), respectively. That is because here we shelve only within (1,1) charge configuration region—far from the (1,1)-(1,2) crossing—where (1,2) states are not available for the transitions.

(ii) As we approach the (1,1)-(1,2) crossing at $\gamma'_{\max} = 0$, we start to observe tunneling between the $|E\rangle$ and $|T_-\rangle$ states—visible as the blue peak in Fig. 2(c). That transition happens as a sequential $|E\rangle \rightarrow |\downarrow S\rangle \rightarrow |T_-\rangle$ tunneling using $|\downarrow S\rangle$ as an intermediate state. The most efficient shelving is taking place for $-\gamma_e B/2 < \gamma'_{\max} < \gamma_e B/2$ (grey region in Fig. 2), as in this region the $|\downarrow S\rangle$ state is exactly between $|E\rangle$ and $|\downarrow\downarrow\rangle$ energy levels [see Fig. 2(a)]. However, due to the thermal broadening of the energy levels, we can also observe some nonzero tunneling for $\gamma'_{\max} < -\gamma_e B/2$. While the excited state $|E\rangle$ maps to $|T_-\rangle$, the ground $|G\rangle$ state does not undergo any tunneling around $\gamma'_{\max} = 0$, apart from a minimal leakage to $|T_-\rangle$ state [small blue peak in Fig. 2(b)] due to the admixture of $\downarrow\uparrow$ spin configuration in $|G\rangle$.

(iii) If we further increase γ'_{\max} , reaching $\gamma'_{\max} > \gamma_e B/2$ region, we start to observe additional tunneling effects. In Fig. 2(b) we can observe the probability of $|G\rangle$ state decreasing and $|\uparrow S\rangle$ and $|T_-\rangle$ states increasing for larger γ'_{\max} values. That happens because for $\gamma'_{\max} > \gamma_e B/2$ the $|\uparrow S\rangle$ energy level falls below the $|G\rangle$ state, opening the $|G\rangle \rightarrow |\uparrow S\rangle$ tunneling path. Then, when we return to (1,1) region in the shelving procedure, the $|\uparrow S\rangle$ state can tunnel back to the $|G\rangle$ or $|\uparrow\uparrow\rangle$ state. Hence the nonzero probability of those three states on the right side of Fig. 2(b). Similarly for the initial $|E\rangle$ state in Fig. 2(c), in the $\gamma'_{\max} > \gamma_e B/2$ region we can observe additional tunneling processes manifesting

themselves as different final shelving probabilities compared to the shaded region. Here the $|\downarrow S\rangle$ level falls below all the (1,1) states at γ'_{\max} [see right side of Fig. 2(a)]. At this point only $|E\rangle \rightarrow |\downarrow S\rangle$ transition is possible. Upon shelving back to (1,1) region the $|\downarrow S\rangle$ state partially tunnels back to $|E\rangle$ and $|T_{-}\rangle$ states, resulting in a final mixture of those three states.

The shaded region of plots Figs. 2(b) and 2(c) gives the best readout visibility, as there the $|G\rangle$ and $|E\rangle$ states are being ultimately mapped to the (0,2) and (1,1) charge configurations, respectively. In the $\gamma'_{\max} > \gamma_e B/2$ region the readout visibility will be harmed by all the additional tunneling effects discussed above. This problem for large γ'_{\max} can be minimized by increasing t_{out} —see Figs. 2(d) and 2(e) where the shelving-out time has been extended to 10 μs . A slower return to the (1,1) region allows the (1,2) states to tunnel back predominantly to the states, which preserve correct readout mapping, i.e., the $|\uparrow S\rangle$ state tunnels back to the $|G\rangle$ state before reaching $|T_{+}\rangle$ and the $|\downarrow S\rangle$ state tunnels back to the $|T_{-}\rangle$ state before reaching $|E\rangle$. Increasing t_{out} for large γ'_{\max} would possibly allow us to reach a similar shelving efficiency as shown for $\gamma'_{\max} \approx 0$. At the same time, however, it increases the total readout time, which results in longer qubit exposure to noise. Thus, it is still more beneficial to perform shelving within the $-\gamma_e B/2 < \gamma'_{\max} < \gamma_e B/2$ region and keep t_{out} short. Other methods to improve the readout efficiency are to use a larger external magnetic field B , which increases the Zeeman splitting between $|E\rangle$ and $|T_{-}\rangle$ states [resulting in wider peaks in Fig. 2(c)], or lower electron temperatures, that can improve the readout by limiting the thermal broadening, making the transition sharper even if the energy levels are very close to each other.

In QDs using a micromagnet or a deterministically polarized nuclear bath, the magnetic field gradient, and thus ΔE_z , can be set at the beginning of the measurements and kept relatively constant throughout the experiment. In donor-based devices, however, ΔE_z originates from the different hyperfine interaction of the electron spins to each donor dot nuclei. As a consequence, due to the presence of nuclear spin flips [22], ΔE_z can change both value and sign, which can result in a reversed mapping of the $|G\rangle$ and $|E\rangle$ states. In Figs. 2(f) and 2(g) we show shelving readout for $\Delta E_z = -300$ MHz, with an opposite sign of ΔE_z compared to the plots (b) and (c). Now it is the ground state $|G\rangle$, which is predominantly in the $|\downarrow\uparrow\rangle$ state and is thus mapped to T_{-} after shelving. At the same time, the $|E\rangle$ state is blocked during the $(1) \rightarrow (2) \rightarrow (1)$ process. After $(1) \rightarrow (3)$ step, the $|E\rangle$ state will be mapped to $|T_0\rangle$ and, due to fast relaxation, ultimately to S(0,2). This step requires staying in point (3) for a time longer than T_0 but shorter than T_{-} relaxation time, which is experimentally feasible [33]. The reverse mapping therefore randomizes the readout process, lowering the overall visibility.

To clarify the impact of the nuclear spin flips, in Fig. 3(a) we show the final probability of blocked triplet states T_{\pm} for simulations with initial states $|G\rangle$ (left) and $|E\rangle$ (right) as a function of ϵ and ΔE_z . Here we used $\gamma'_{\max} = 0$ and both positive and negative values of ΔE_z . As explained above, for positive ΔE_z it is the excited qubit state $|E\rangle$, which is mapped to $|T_{-}\rangle$ and eventually to the (1,1) charge configuration,

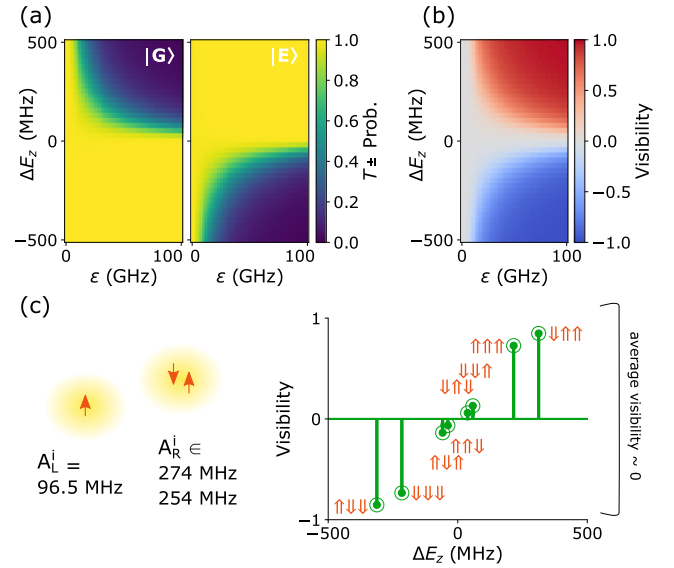


FIG. 3. Impact of nuclear spins on shelving readout visibility. (a) Final probability of blocked triplet states T_{-} and T_{+} after shelving as a function of detuning ϵ and Zeeman energy difference ΔE_z . Left (right) plot corresponds to simulations starting from the ground $|G\rangle$ (excited $|E\rangle$) eigenstates. These results highlight the reverse mapping of $|G\rangle$ singlet-like and $|E\rangle$ triplet-like states for positive and negative ΔE_z . (b) Visibility of shelving readout as a function of ϵ and ΔE_z . (c) Visibility of shelving readout for all possible nuclear configurations for an example of 1P-2P system at $\epsilon = 50$ GHz. Due to the reverse readout mapping for positive and negative ΔE_z , the visibility averaged over all nuclear configurations comes to approx. 0.

while for negative ΔE_z it is the $|G\rangle$ state. In Fig. 3(b) we plot the readout visibility using the mapping of $\Delta E_z > 0$, thus the visibility of the lower part of the plot is negative (more details on visibility calculations in Appendix). We can see the absolute value of the visibility increases with $|\Delta E_z|$ —that is due to smaller $\downarrow\uparrow$ and $\uparrow\downarrow$ mixing and hence less leakage. The visibility reaches 0 for $\Delta E_z = 0$ because both $|G\rangle$ and $|E\rangle$ states, now corresponding to singlet (1,1) and triplet T_0 states, respectively, can transfer to $|\downarrow S\rangle$ state equally fast. The visibility is also reduced for small detuning ϵ , as in this region the exchange interaction dominates over ΔE_z (the x axis limits $\epsilon = 0$ and 100 GHz correspond to exchange J values of 2 GHz and 40 MHz, respectively).

We assume quasistatic nuclear polarization, which means that the nuclear spins are not flipping during single qubit operations and shelving readout. However, as the full experiment time usually reaches minutes or even hours, the nuclear spins will likely flip multiple times. In the system of two donor quantum dots we can express all possible values of ΔE_z as

$$\Delta E_z = \sum_{j=1}^{N_R} A_R^j I_{Rz}^j - \sum_{i=1}^{N_L} A_L^i I_{Lz}^i \quad (1)$$

where i and j enumerate nuclear spins in left and right dots, with total donor numbers N_L and N_R , respectively. A_L^i (A_R^j)

is the hyperfine constant of the i th (j th) donor in left (right) dot and I_{Lz}^i (I_{Rz}^j) is the i th left-dot (right-dot) nuclear spin polarization in z direction and can take values of $\pm 1/2$. The number of possible ΔE_z values therefore increases with the number of donors as $2^{N_L+N_R}$.

In Fig. 3(c) we show the impact of the dynamic nuclear spins in an example of a 1P-2P system with hyperfine constants $A_L = 96.5$ MHz and $A_R^j \in [274, 254]$ MHz, as observed in a recent device of Ref. [35]. The 1P-2P system allows 8 different values of ΔE_z within the range between -312.25 and 312.25 MHz. We plot the visibility for all the different possible nuclear spin configurations, which after averaging over all the nuclear spin states goes to approximately zero. Although these results show one specific example of a multidonor dot, the average zero visibility will be common to all quantum dots with multiple donors (with any values of hyperfine constants) due to the inherent symmetry of the system. This is because for any particular nuclear configuration with a given ΔE_z it is possible to get the opposite value of ΔE_z just by flipping all the nuclear spins. Additionally, even if nuclear polarization is changing slower than the total experiment time, it is important to know the sign of ΔE_z to ensure a proper mapping of $|G\rangle$ and $|E\rangle$ to $(0,2)$ and $(1,1)$ charge configurations. Until now only the absolute value of ΔE_z has been considered in relevant experiments in donor-based devices [36].

C. Calibration step of a shelved readout

The zero visibility of shelving readout in donor-based systems can be mitigated if the nuclear spins are deterministically initialized at each shot, setting ΔE_z the same for every measurement using either nuclear magnetic resonance (NMR) or dynamic nuclear polarisation (DNP) [37,38]. Here we propose a method to greatly increase shelving readout visibility for donor-based devices through the addition of an extra calibration step before every qubit measurement—shown schematically in Fig. 4. The step consists of initializing the system in the $(1,1)$ ground state $|G\rangle$ [by an adiabatic sweep from negative to positive ϵ starting from the $S(0,2)$ state] and then conducting shelving readout with such a prepared initial state. The result of the shelving readout— $(1,1)$ or $(0,2)$ signal—determines if the ground state is predominantly in $\uparrow\downarrow$ or $\downarrow\uparrow$ state and thus specifies the sign of ΔE_z . The following qubit operation can then use this information via a feed-forward protocol to map the final readout results. This proposal requires that nuclear spin polarization is changing considerably slower than the qubit operation time. Due to seconds-long nuclear spin coherence times [2,3], this is a reasonable assumption for systems based on phosphorus donors in silicon. In practice it can differ depending on number of donors and electrons in the system due to ionization shock [22]. For the 1P-2P case shown in Fig. 3(c) the calibration step would increase the visibility at detuning $\epsilon = 50$ GHz from 0 to 44%—equivalent to fidelity of 72% (see Appendix). Readout fidelity of over 99% can be achieved when we increase detuning ϵ to 800 GHz. Such values of detuning are experimentally feasible [28], however they can still be minimized if needed, by using lower temperatures or higher magnetic fields. In the limit of very high detuning only nuclear spin con-

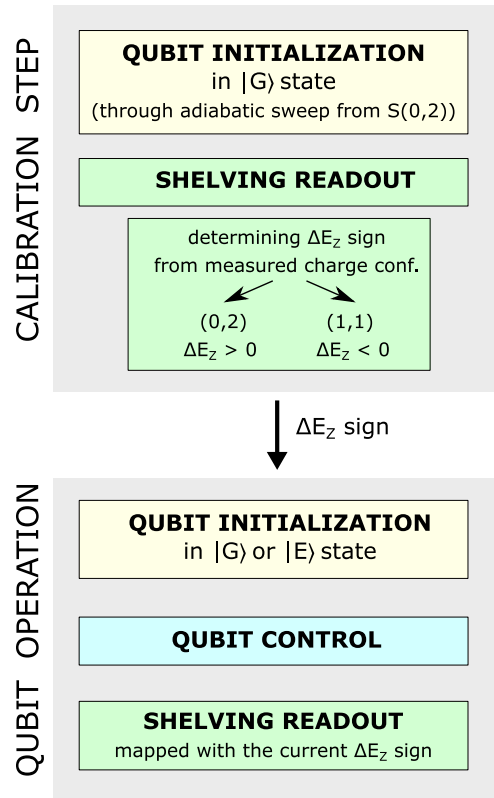


FIG. 4. Scheme of the calibration step protocol. The calibration step includes initializing the qubit in $|G\rangle$ state, performing shelving readout and using the final measured charge configuration to obtain information about current ΔE_z sign. The information can be further used in subsequent qubit operation to determine the correct mapping for shelving readout.

figurations with $\Delta E_z \approx 0$ would give zero visibility, harming the total efficiency of shelving readout. Those configurations can be avoided by fabricating multidonor quantum dots with hyperfine constants A_L^i, A_R^j , which can never add up to give $\Delta E_z = 0$, such as $A_L^1 = A_R^1 = A_R^2$ for the 1P-2P system.

IV. LATCHING

A. Latching readout protocol

Latching readout [30] provides an alternative means to greatly increase the signal contrast between singlet and triplet states, compared to either PSBR or shelving, as the final charge states that are measured— $(0,2)$ and $(1,2)$ —now differ by one electron. This difference creates a much larger charge signal for a charge sensor in comparison to that achievable for the $(1,1)$ - $(0,2)$ dipole. In addition, latching is insensitive to the sign of the magnetic field gradient as it always maps the ground, singlet-like state to the $(0,2)$ and excited, triplet-like state to the $(1,2)$ charge configuration. While latched readout gives an improved readout signal contrast, its efficiency can still be compromised by the triplet relaxation process. Here we investigate this relaxation process in which the excited, triplet-like $|E\rangle$ state is subject both to the standard $T_0 - S$ relaxation, as well as fast charge relaxation via $S(1,1) - S(0,2)$, since ΔE_z introduces an admixture of the singlet state in $|E\rangle$ [11].

Latching is therefore more efficient at small magnetic field gradients and requires a large differential tunneling between each of the dots and the reservoir, so that electron tunneling to and from the SET for one of the QDs is enabled and for the other QD is suppressed.

The latched readout protocol is schematically shown in Figs. 1(b) (blue arrows) and 1(e). First the system is detuned from (1,1) to the Pauli blocked (0,2) region during the (1) \rightarrow (2) process. This transition needs to be adiabatic to allow $|G\rangle$ to tunnel to $S(0,2)$, but fast enough to avoid triplet relaxation, $t_{\text{ramp}} < T_{\text{relax}}$. Next, γ is very quickly increased to point (3) in the (1,2) region. The system is kept there for a t_{wait} time where the charge state of the quantum dots is measured. At point (3) the $|E\rangle$ state maps to the (1,2) charge configuration due to electron tunneling from the SET to the right dot. To preserve the contrast between (1,2) and (0,2) states tunneling from the SET to the left dot needs to be suppressed. This means that the t_{wait} time needs to be considerably larger than $1/\Gamma_R$ but smaller than $1/\Gamma_L$.

B. Triplet state relaxation

Latching readout is still subject to similar relaxation mechanisms, which affect Pauli blockade readout [11]. However, with the latching protocol this relaxation only happens until an electron tunnels from the SET to the right dot, mapping $|E\rangle$ to some (1,2) state. This tunneling time can be minimized to limit the harming effect of the relaxation compared to PSBR. Since ΔE_z mixes singlet and triplet states, the relaxation rate of $|E\rangle \rightarrow S(0,2)$ can be expressed as

$$\Gamma_E = \Gamma_T |\langle E|T_0\rangle|^2 + \Gamma_S |\langle E|S(1,1)\rangle|^2 \quad (2)$$

where Γ_T and Γ_S are T_0 and $S(1,1)$ relaxation rates, respectively. Because $\Gamma_T \ll \Gamma_S$, due to spin conservation, the relaxation becomes much faster when there is a considerable admixture of $S(1,1)$ in $|E\rangle$ state, which typically occurs for large Zeeman energy difference ΔE_z .

The relaxation in donor system originates from the deformation potential of the crystal lattice [39,40]. The $S(1,1)$ - $S(0,2)$ energy difference in our calculations is of the order of 1–100 GHz hence only acoustic phonons are emitted during relaxation. Charge relaxation due to the deformation potential is proportional to ϵ^{D-2} where D is 2 for 2D and 3 for 3D phonons [41]. Considering the large size (on the order of 100 nm in each direction) of the silicon crystal hosting the donor QDs, we can assume 3D phonons will dominate in our devices and we therefore adopt a relaxation rate proportional to $|\epsilon|$. The predicted singlet and triplet relaxation rates will take the form $\Gamma_T = \Gamma_T^0 C |\epsilon|$ and $\Gamma_S = \Gamma_S^0 C |\epsilon|$, with C being coefficient determining relaxation dependency on detuning. The exact values of Γ_T^0 , Γ_S^0 , and C are dependent on the specific device under consideration, hence here we treat them as free parameters to optimize the readout visibility in the next section. We investigate the qualitative effects the relaxation has on the latched readout efficiency and we explore different ranges of the relaxation rates with respect to the SET-QD tunneling rates.

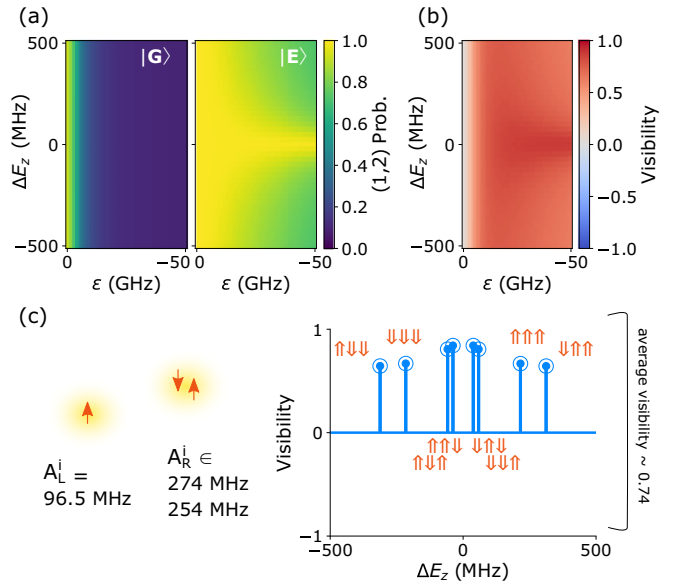


FIG. 5. Latched readout visibility. (a) Final probability of the (1,2) charge configuration after latching as a function of detuning ϵ and the Zeeman energy difference ΔE_z . Left (right) plot corresponds to simulations starting from ground the $|G\rangle$ (excited $|E\rangle$) eigenstates. (b) Visibility of latching readout as a function of ϵ and ΔE_z . (c) Visibility of latched readout for all possible nuclear configurations for an example of a 1P-2P system at $\epsilon = -50$ GHz.

C. Latching visibility

We model the latched readout by simulation of the (2) \rightarrow (3) process in Fig. 1(b) (blue arrows). We start at $\gamma'_{\text{min}} = -100$ GHz, move to $\gamma'_{\text{max}} = 100$ GHz within t_{in} time, and wait at γ'_{max} for a time t_{wait} . In Fig. 5(a) we plot the final probability of the (1,2) charge configuration for the initial state $|G\rangle$ (left) and $|E\rangle$ (right) as a function of ϵ and ΔE_z . We assume that in point 2 (blue) in Fig. 1(b) the $|G\rangle$ state has evolved to $S(0,2)$, and we set initial probabilities for the simulation accordingly. The parameters used for simulations are following $(\Gamma_L, \Gamma_R, \Gamma_S^0, \Gamma_T^0, C, t_{\text{in}}, t_{\text{wait}}) = (10^5 \text{ s}^{-1}, 10^7 \text{ s}^{-1}, 10^7 \text{ s}^{-1}, 10^5 \text{ s}^{-1}, 1/50 \text{ GHz}^{-1}, 1 \text{ ns}, 500 \text{ ns})$. A key feature of the plot is that the (1,2) probabilities are symmetric with respect to the $\Delta E_z = 0$ axis. The readout visibility in Fig. 5(b) is therefore now insensitive to the sign of ΔE_z , which means the readout mapping is the same both for positive and negative magnetic field gradients. Therefore, in contrast to shelving readout, latched readout does not need to be calibrated as it gives a nonzero average visibility for donor systems even if the nuclear spins are flipping during the experiment. In Fig. 5(c) we plot the visibility for all the possible nuclear configurations in the 1P-2P qubit system [discussed previously in Fig. 3(c)], for the detuning $\epsilon = -50$ GHz. The average visibility for this specific configuration and parameter set reaches 74%—equivalent to fidelity of 87% (see Appendix). Further in the text we explain how this value can be improved.

There are two effects that harm the latched readout visibility, which can be observed in Fig. 5(a). The first one is the $|E\rangle$ to $S(0,2)$ state relaxation, which is reflected in the decreased (1,2) probability (green regions) in the right plot. For zero

ΔE_z the $|E\rangle$ state is a pure triplet, with no singlet admixtures, thus only the triplet relaxation Γ_T will contribute to the full relaxation rate. However, within the detuning range plotted, the Γ_T relaxation rate we adapt (max. $\Gamma_T^0 C|\epsilon| = 10^5 \text{s}^{-1}$ for $\epsilon = -50 \text{GHz}$) is considerably slower than $(1, 1) \rightarrow (1, 2)$ tunneling rate $\Gamma_R = 10^7 \text{s}^{-1}$ and thus not visible in Fig. 5(a). For nonzero ΔE_z the singlet relaxation Γ_S starts to play a role, as ΔE_z introduces $S(0, 2)$ admixtures into the $|E\rangle$ state. For the set of parameters that we use in the simulations the singlet relaxation rate Γ_S reaches the same value as $(1, 1) \rightarrow (1, 2)$ tunneling rate, $\Gamma_S = \Gamma_R$, at a detuning of -50GHz . The total $|E\rangle$ relaxation effects will increase both with $|\Delta E_z|$ [due to larger admixtures of $S(1,1)$ in $|E\rangle$ state] and $|\epsilon|$ (as Γ_S is linearly dependent on detuning)—hence the shape of the green regions in the right plot in Fig. 5(a). The second effect limiting latched readout visibility is leakage of the ground singlet state $|G\rangle$ to the $(1,2)$ states at small, up to few GHz, detuning $|\epsilon|$. This leakage channel can be observed in the left plot of Fig. 5(a) as a brighter region—increased $(1,2)$ probability—close to $\epsilon = 0$. For small $|\epsilon|$ we are still within the $S(0, 2) - S(1, 1)$ anticrossing region, where the charge configuration of the ground singlet state is not well defined. While the $S(0, 2) \rightarrow (1, 2)$ transition is nearly blocked (due to the small tunneling rate Γ_L), the $S(1,1)$ part of the wavefunction can still tunnel to the $(1,2)$ states upon latching. As we move away from $(1,1)-(0,2)$ anticrossing by increasing $|\epsilon|$ the $S(1,1)$ admixture into the ground singlet state decreases and this leakage effect vanishes.

If it were not for the $|G\rangle \rightarrow (1, 2)$ leakage effect, it would be preferable to use arbitrarily small $|\epsilon|$ to minimize the $|E\rangle$ relaxation. Similarly, if not for the $|E\rangle \rightarrow S(0, 2)$ relaxation, an arbitrarily large $|\epsilon|$ would be preferable to avoid the $|G\rangle \rightarrow (1, 2)$ leakage. The presence of the two competing leakage effects requires a careful optimization to reach the maximum possible latched readout visibility. To achieve $>99\%$ fidelity it is necessary to optimize the qubit design both at fabrication and measurement level to simultaneously minimize both the relaxation and leakage effects—we discuss this in detail in the next section.

D. Optimization of readout parameters

Optimization of the latched readout protocol can therefore be ensured at two points during the system design. First, the potential for high readout visibility can be optimized during the STM fabrication process. The device can be engineered for best readout performance by determining and setting the number of donors in each quantum dot, the tunnel coupling between dots and the tunnel rates between the SET and the dots. Secondly, optimization can occur during singlet-triplet qubit operation. For a device of a specific architecture and system parameters the experimental variables like ϵ , t_{in} , t_{wait} can be adjusted to minimize the effect of relaxation processes to achieve the highest visibility possible.

First we discuss optimization at the qubit design. The main problem limiting latched readout efficiency is the $|E\rangle \rightarrow S(0, 2)$ relaxation due to singlet admixtures in $|E\rangle$ state introduced by ΔE_z . A straightforward way to improve the visibility is then to minimize the hyperfine interaction, which will result in decreased ΔE_z . To achieve this we can use quantum dots

with a larger inter-donor separation, thereby weakening the electron localization at the donor sites and thus decreasing the hyperfine constants [42]. Another solution is to load the system with more electrons, e.g., $(1,3)$ instead of $(1,1)$ for the 1P-2P system, where the lower electron pair on the right dot does not take part in spin dynamics but screens the hyperfine interaction of the single outer electron. Although donor placement can be currently performed with great accuracy [4], fabrication of multidonor dots with precise control over the donor positions within a single lithographic patch is the focus of ongoing work. Currently, the characteristics of the donor dots can be derived from postfabrication measurements combined with atomistic modeling [43,44], allowing one to select qubits, which are most suitable for latched readout. Also, flexibility of loading more or less electrons to each fabricated multidonor dot makes them less vulnerable to uncertainty in donor placements. In the long term, promising ongoing projects in our team [45] and others [46–48] remain focused on deterministic incorporation of donors such that their number and position is precisely controlled at the fabrication stage. We know a nonzero ΔE_z is necessary for qubit operation and thus can not be entirely removed. The charge relaxation due to singlet admixtures in the $|E\rangle$ state will therefore always be the limiting factor of latched readout. It is therefore important to also maximize the $(1,1)-(1,2)$ transition rate, Γ_R by bringing the right QD as close as possible to the SET. Ideally $\Gamma_S \ll \Gamma_R$, so the tunneling of the $|E\rangle$ state to $(1,2)$ happens much faster than its relaxation to $(0,2)$. It is also important to minimize Γ_L to avoid any undesired $(0,2)-(1,2)$ tunneling, which would decrease $|G\rangle$ state visibility. One way this can be achieved is by placing the left donor QD further away from SET. Additionally, using a larger inter-dot distance—and thus smaller tunneling t_0 between the dots—helps latched readout, since it makes the leakage region from the left plot in Fig. 5(a) narrower as well as suppresses $|E\rangle \rightarrow S(0, 2)$ relaxation [41,49].

In Fig. 6(a) we show the latched readout fidelity averaged over all possible nuclear spin configurations for the 1P-2P system [hyperfine constants, detuning and relaxation rates as in Fig. 5(c)] as a function of the ratio Γ_L/Γ_R . Here we keep Γ_R constant while changing the tunneling rate of the left dot Γ_L ; and we plot the fidelity for three different values of Γ_R (for each value we adjust the latching time to $t_{\text{wait}} = 5/\Gamma_R$). We can see that the readout efficiency drastically falls when the ratio Γ_L/Γ_R approaches one, i.e., when the tunnel rates between each dot and the SET are the same. In this limit no latching effects occur and both $|G\rangle$ and $|E\rangle$ states are equally mapped to $(1,2)$ charge configuration. The fidelity improves for smaller Γ_L/Γ_R ratios, with maximum fidelity to be achieved at the limit of $\Gamma_L/\Gamma_R \rightarrow 0$. However, we can see in Fig. 6(a) that the fidelity saturates already around $\Gamma_L/\Gamma_R = 10^{-4}$. We can also notice the fidelity improves when increasing Γ_R . As the relaxation rate here is set constant at $\Gamma_S = 10^7 \text{s}^{-1}$, increasing Γ_R over this value allows the tunneling to exceed the relaxation effect. However, even for $\Gamma_S = \Gamma_R$ we still can achieve fidelity values of over 90%—ultimately too little for high-fidelity singlet-triplet qubit operation but useful as a tool for further investigation of relaxation rates.

Once the system is optimized at the fabrication level we can further improve the latched readout fidelity by choosing

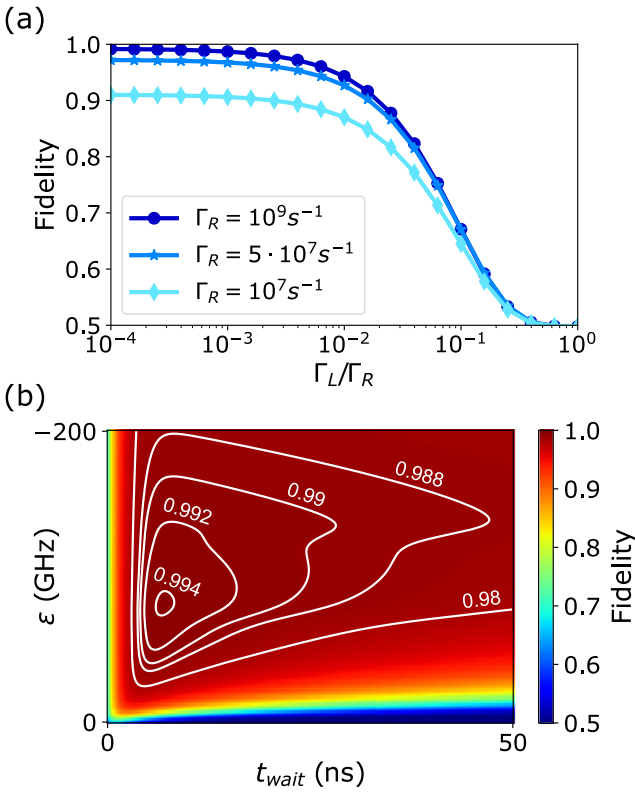


FIG. 6. Optimization of latched readout fidelity for the 1P-2P donor qubit. (a) Average readout fidelity as a function of ratio Γ_L/Γ_R for three different values of Γ_R . For each Γ_R value the wait time is adjusted to $t_{\text{wait}} = 5/\Gamma_R$. All other parameters (hyperfine constants, detuning, relaxation rates) are same as for Fig. 5(c). (b) Fidelity as a function of t_{wait} and ϵ for $\Gamma_R = 10^9 \text{ s}^{-1}$, $\Gamma_L = 10^5 \text{ s}^{-1}$.

the optimal values of ϵ and t_{wait} during the measurement. Here we discuss the example of 1P-2P qubit system of Fig. 5(c). We limit the optimization at the fabrication level to increasing Γ_R to 10^9 s^{-1} . That ensures a low $\Gamma_L/\Gamma_R = 10^{-4}$ ratio and high value of Γ_R with respect to relaxation rates. In Fig. 6(b) we show the average fidelity for the described 1P-2P system as a function of t_{wait} and ϵ . We can see that within a relatively small range of both parameters the fidelity varies between 50 and a maximum of over 99%. The lowest readout efficiency can be observed for small t_{wait} of less than ns (which is on the order of tunneling time $1/\Gamma_R$) due to an insufficient time for $(1,1) \rightarrow (1,2)$ tunneling, and for detuning values close to zero, due to $(0,2) \rightarrow (1,1)$ leakage. If we increase both t_{wait} and ϵ , the fidelity improves significantly. It is possible to identify a value around $\epsilon \approx -80$ GHz and $t_{\text{wait}} \approx 6.9$ ns that minimizes the two competing relaxation processes, resulting in maximum fidelity of 99.4%. However, if we further increase either t_{wait} or ϵ , we can see the fidelity deteriorates again due to the increased triplet relaxation. Thus the optimization during the measurement is finding the sweet spot of t_{wait} or ϵ , which maximizes the latched readout visibility.

V. g -FACTOR DIFFERENCE

Finally, we would like to comment on other possible source of ΔE_z in donor systems, namely the g -factor difference

between the dots. This g -factor variability originating from spin-orbit effects has been widely discussed for gate-defined quantum dots [20,21]. ΔE_z of the order of 10 MHz/T has been recently measured in silicon dots [50]. As the value of g factor in quantum dots may vary with electric fields [51] and due to atomistic effects, like interface roughness, it is also adequate to consider the same effects in donor dots. The g -factor shift due to electric field has been investigated theoretically for a single donor [52], showing that relative g shifts of the order of $10^{-5} - 10^{-4}$ are possible for experimentally realistic values of magnetic and electric fields. Also number of donors in the dots and atomistic arrangement within the dot may have an effect on the g -factor values, however the information on that matter is limited. Previous measurements of 1P and 2P dots reported g -factor values within error of each other, i.e., $g_{1P} = 1.988 \pm 0.002$ and $g_{2P} = 1.986 \pm 0.002$ [35]. As we are not able to precisely estimate the g -factor difference in a system of two arbitrary multidonor dots, we consider only nuclear-spin related ΔE_z in this paper. However, we can qualitatively discuss how the g -factor difference of various magnitude could potentially impact both shelving and latching readout protocols.

The Zeeman energy difference due to g -factor difference Δg between the dots is equal

$$\Delta E_g = \frac{\Delta g}{g_0} h \gamma_e B \quad (3)$$

where g_0 is an average g factor of both dots, B is external, static magnetic field, and $\gamma_e = 27.97$ GHz/T is electron spin gyromagnetic ratio. The total Zeeman energy difference in the system would then be a sum of the effects originating from g factors and nuclear spins

$$\Delta E_{\text{tot}} = \Delta E_g + \Delta E_z. \quad (4)$$

While we have shown ΔE_z changes in time and takes both positive and negative values, we can assume ΔE_g is constant in time. Then, for 1P-2P example discussed in this paper ΔE_{tot} would take all the possible values of ΔE_z [shown in Figs. 3(c) and 5(c)] shifted by ΔE_g value. Here we can consider two regimes:

(i) $|\Delta E_g| < \max(\Delta E_z)$ —in this case ΔE_{tot} would take both positive and negative values, however in contrast to ΔE_z its set will not be symmetrical with respect to 0. For shelving readout that would mean some improvement in fidelity, increasing the average visibility to >0 . However, in general the improvement would not be sufficient to achieve high-fidelity readout without calibration step. The fidelity of readout + calibration step would not change significantly when ΔE_g is included, as some of the absolute values of Zeeman energy difference will increase (beneficial for shelving readout) and some will decrease (detrimental to the readout) as compared to no g -factor difference. Similarly for latched readout, simultaneous increase of some absolute values of Zeeman energy difference and decrease of others will mitigate the effect on readout fidelity. Exact changes in readout visibilities will be dependent on exact values of hyperfine constants and need to be calculated case-by-case.

This regime assumes ΔE_g up to few hundreds MHz, which translates to approximately $g/g_0 < 10^{-3}$ for realistic values of magnetic field and hyperfine interaction in multidonor dots.

(ii) $|\Delta E_g| > \max(\Delta E_z)$ —here ΔE_{tot} would take only negative or only positive values (depending on the sign of ΔE_g). That would have positive effect on shelving readout, as the high-fidelity limit could be now achievable without a need for calibration step. In contrast, that high ΔE_g would be detrimental for latched readout, as generally increased absolute values of the Zeeman energy difference would magnify the effect of triplet relaxation.

This regime spans g/g_0 values above approximately $>10^{-3}$.

Exact calculations for a given value of g -factor difference can be performed with our model by including ΔE_g in the Hamiltonian. The magnitude of ΔE_g might determine, which of the two discussed readout protocols is more favourable for a given device.

VI. CONCLUSIONS

We have investigated two singlet-triplet qubit readout methods, namely shelving and latched readout, applied to multiphosphorus donor qubits in silicon. We performed numerical simulations to estimate the readout visibility for realistic multidonor quantum dot qubits and analyzed the influence of different system parameters (tunneling rates, timescales of the experiment, hyperfine interaction) on the maximum readout fidelity, which can be achieved. For shelving readout we showed that the dynamic nature of nuclear spin flipping (at the frequency of the order of Hz) gives rise to a zero visibility of the singlet-triplet states. To overcome that it is essential to incorporate a calibration step in which we probe the nuclear spins before each measurement protocol. Using such a calibration step we were able to show that the readout fidelity could be increased to over 99% when correct, i.e., corresponding to the current nuclear state, readout mapping is applied. In contrast, latched readout is not sensitive to the dynamic nature of the nuclear spin flipping because it maps singlet and triplet states the same way for both positive and negative ΔE_z . As a consequence we showed that by optimizing both the device design and operating conditions we could achieve 99% fidelity in 1P-2P system.

ACKNOWLEDGMENTS

This research was conducted by the Australian Research Council Centre of Excellence for Quantum Computation and Communication Technology (CE170100012), the US Army Research Office under Contract No. W911NF-17-1-0202 and Silicon Quantum Computing Pty Ltd.

The research was undertaken with the assistance of resources and services from the National Computational Infrastructure (NCI) under an NCMAS 2021 allocation, supported by the Australian Government, and of the computational cluster Katana supported by Research Technology Services at UNSW Sydney.

APPENDIX: METHODS

We first calculate two-electron eigenstates of the system. In the basis $[S(0, 2), \uparrow\uparrow(1, 1), \uparrow\downarrow(1, 1), \downarrow\uparrow(1, 1), \downarrow\downarrow(1, 1)]$

we can express the Hamiltonian in the following way:

$$H_{2e} = h \begin{pmatrix} \epsilon & 0 & t_0/\sqrt{2} & -t_0/\sqrt{2} & 0 \\ 0 & \gamma_e B & 0 & 0 & 0 \\ t_0/\sqrt{2} & 0 & -\frac{\Delta E_z}{2} & 0 & 0 \\ -t_0/\sqrt{2} & 0 & 0 & \frac{\Delta E_z}{2} & 0 \\ 0 & 0 & 0 & 0 & -\gamma_e B \end{pmatrix}. \quad (\text{A1})$$

The three-electron (1,2) states $[\uparrow S, \downarrow S]$ are independent and can be described by Hamiltonian:

$$H_{3e} = h \begin{pmatrix} \frac{\epsilon}{2} - \gamma + \frac{\gamma_e B}{2} & 0 \\ 0 & \frac{\epsilon}{2} - \gamma - \frac{\gamma_e B}{2} \end{pmatrix}. \quad (\text{A2})$$

Here h is Planck constant, B is external, static magnetic field, and $\gamma_e = 27.97$ GHz/T is electron spin gyromagnetic ratio. For all the calculations in the paper we use tunneling $t_0 = -2$ GHz and external magnetic field $B = 2$ T.

The two-electron basis states $\uparrow\uparrow$ and $\downarrow\downarrow$ are not mixed with any other states in the Hamiltonian and form two eigenstates T_+ and T_- , respectively. $S(0,2)$ state mixes with $\uparrow\downarrow$ and $\downarrow\uparrow$, forming three eigenstates: S_{02} , G , and E . S_{02} consists predominantly of $S(0,2)$ basis state, however gets some admixture of (1,1) state around the (0,2)-(1,1) anticrossing. At zero ΔE_z the G and E eigenstates can be described as singlet and triplet states: $|G\rangle \approx (\uparrow\downarrow - \downarrow\uparrow)/\sqrt{2}$ and $|E\rangle = (\uparrow\downarrow + \downarrow\uparrow)/\sqrt{2}$.

The exchange J is defined in the paper as the energy difference between the lowest singlet and unpolarized triplet states, i.e., between $|G\rangle$ and $|E\rangle$ states when $\Delta E_z = 0$. It arises from mixing of the singlet (1,1) and the (0,2) states. As $S(0,2)$ is included in the basis of Hamiltonian H_{2e} , we do not need to explicitly introduce J between $\uparrow\downarrow(1, 1)$ and $\downarrow\uparrow(1, 1)$ states, but we obtain J when solving H_{2e} for eigenstates. J then is dependent on detuning ϵ , such that it reaches a value of t_0 for $\epsilon = 0$ and goes to 0 for $\epsilon \rightarrow \infty$.

We simulate shelving and latching readout solving equation

$$\frac{dP}{dt} = \Gamma P \quad (\text{A3})$$

where P is a vector of eigenstates probabilities and Γ is a matrix of transition rates. The rates in Γ depend on ϵ and γ thus in our simulations are effectively time-dependent. The same problem can be solved with master equation in Lindblad form, however that approach would give the same results as we do time evolution in the basis of eigenstates.

We calculate transition rates between each two-electron and three-electron states using Fermi's golden rule:

$$\Gamma_{\Psi \rightarrow \uparrow S} = (\Gamma_L |\langle \Psi | S(0, 2) \rangle|^2 + \Gamma_R (|\langle \Psi | \uparrow\uparrow \rangle|^2 + |\langle \Psi | \uparrow\downarrow \rangle|^2)) \times f((E_\Psi - E_{\uparrow S}), T, \mu),$$

$$\Gamma_{\Psi \rightarrow \downarrow S} = (\Gamma_L |\langle \Psi | S(0, 2) \rangle|^2 + \Gamma_R (|\langle \Psi | \downarrow\uparrow \rangle|^2 + |\langle \Psi | \downarrow\downarrow \rangle|^2)) \times f((E_\Psi - E_{\downarrow S}), T, \mu),$$

where $f()$ is Fermi-Dirac distribution, T is temperature and μ is chemical potential of the SET. In all the calculations in the text we use $T = 200$ mK and $\mu = 0$.

The visibility of the readout is calculated as $V = F_G + F_E - 1$, where F_G (F_E) is a final probability of charge configurations corresponding to G (E) state when the initial state of the simulation has been set to G (E). For shelving, F_G is calculated as a sum of final probabilities of S_{02} , G, and E states $F_G = P_{S_{02}} + P_G + P_E$, as we assume all of those states will be mapped to (0,2) charge configuration when we decrease de-

tuning to Pauli blockaded (0,2) region and wait T_0 relaxation time. F_E is calculated as a sum of blocked triplet states T_- and T_+ probabilities. For latching, F_G is final probability of S_{02} state and F_E is a sum of probabilities of (1,2) states i.e., $\downarrow S$ and $\uparrow S$.

Readout fidelity F can be calculated using the visibility V and the relation $F = (V + 1)/2$.

-
- [1] B. E. Kane, A silicon-based nuclear spin quantum computer, *Nature (London)* **393**, 133 (1998).
- [2] J. T. Muhonen, J. P. Dehollain, A. Laucht, F. E. Hudson, R. Kalra, T. Sekiguchi, K. M. Itoh, D. N. Jamieson, J. C. McCallum, A. S. Dzurak, and A. Morello, Storing quantum information for 30 seconds in a nanoelectronic device, *Nat. Nanotechnol.* **9**, 986 (2014).
- [3] T. F. Watson, B. Weber, Y.-L. Hsueh, L. C. L. Hollenberg, R. Rahman, and M. Y. Simmons, Atomically engineered electron spin lifetimes of 30 s in silicon, *Sci. Adv.* **3**, e1602811 (2017).
- [4] M. Fuechsle, J. A. Miwa, S. Mahapatra, H. Ryu, S. Lee, O. Warschkow, L. C. L. Hollenberg, G. Klimeck, and M. Y. Simmons, A single-atom transistor, *Nat. Nanotechnol.* **7**, 242 (2012).
- [5] J. J. Pla, K. Y. Tan, J. P. Dehollain, W. H. Lim, J. J. L. Morton, D. N. Jamieson, A. S. Dzurak, and A. Morello, A single-atom electron spin qubit in silicon, *Nature (London)* **489**, 541 (2012).
- [6] L. Fricke, S. J. Hile, L. Kranz, Y. Chung, Y. He, P. Pakkiam, M. G. House, J. G. Keizer, and M. Y. Simmons, Coherent control of a donor-molecule electron spin qubit in silicon, *Nat. Commun.* **12**, 3323 (2021).
- [7] E. Rashba and V. Sheka, Electric-dipole spin resonances, in *Landau Level Spectroscopy*, Modern Problems in Condensed Matter Sciences, Vol. 27, edited by G. Landwehr and E. Rashba (Elsevier, Amsterdam, 1991), pp. 131–206
- [8] E. A. Laird, C. Barthel, E. I. Rashba, C. M. Marcus, M. P. Hanson, and A. C. Gossard, Hyperfine-Mediated Gate-Driven Electron Spin Resonance, *Phys. Rev. Lett.* **99**, 246601 (2007).
- [9] J. Levy, Universal Quantum Computation with Spin-1/2 Pairs and Heisenberg Exchange, *Phys. Rev. Lett.* **89**, 147902 (2002).
- [10] J. R. Petta, A. C. Johnson, J. M. Taylor, E. A. Laird, A. Yacoby, M. D. Lukin, C. M. Marcus, M. P. Hanson, and A. C. Gossard, Coherent manipulation of coupled electron spins in semiconductor quantum dots, *Science* **309**, 2180 (2005).
- [11] J. M. Taylor, J. R. Petta, A. C. Johnson, A. Yacoby, C. M. Marcus, and M. D. Lukin, Relaxation, dephasing, and quantum control of electron spins in double quantum dots, *Phys. Rev. B* **76**, 035315 (2007).
- [12] C. Barthel, D. J. Reilly, C. M. Marcus, M. P. Hanson, and A. C. Gossard, Rapid Single-Shot Measurement of a Singlet-Triplet Qubit, *Phys. Rev. Lett.* **103**, 160503 (2009).
- [13] B. M. Maune, M. G. Borselli, B. Huang, T. D. Ladd, P. W. Deelman, K. S. Holabird, A. A. Kiselev, I. Alvarado-Rodriguez, R. S. Ross, A. E. Schmitz *et al.*, Coherent singlet-triplet oscillations in a silicon-based double quantum dot, *Nature (London)* **481**, 344 (2012).
- [14] M. D. Shulman, O. E. Dial, S. P. Harvey, H. Bluhm, V. Umansky, and A. Yacoby, Demonstration of entanglement of electrostatically coupled singlet-triplet qubits, *Science* **336**, 202 (2012).
- [15] X. Wu, D. R. Ward, J. R. Prance, D. Kim, J. K. Gamble, R. T. Mohr, Z. Shi, D. E. Savage, M. G. Lagally, M. Friesen *et al.*, Two-axis control of a singlet-triplet qubit with an integrated micromagnet, *Proc. Natl. Acad. Sci. USA* **111**, 11938 (2014).
- [16] P. Harvey-Collard, N. T. Jacobson, M. Rudolph, J. Dominguez, G. A. Ten Eyck, J. R. Wendt, T. Pluym, J. K. Gamble, M. P. Lilly, M. Pioro-Ladrière, and M. S. Carroll, Coherent coupling between a quantum dot and a donor in silicon, *Nat. Commun.* **8**, 1029 (2017).
- [17] P. Pakkiam, A. V. Timofeev, M. G. House, M. R. Hogg, T. Kobayashi, M. Koch, S. Rogge, and M. Y. Simmons, Single-Shot Single-Gate rf Spin Readout in Silicon, *Phys. Rev. X* **8**, 041032 (2018).
- [18] M. F. Gonzalez-Zalba, S. Barraud, A. J. Ferguson, and A. C. Betz, Probing the limits of gate-based charge sensing, *Nat. Commun.* **6**, 6084 (2015).
- [19] J. M. Hornibrook, J. I. Colless, A. C. Mahoney, X. G. Croot, S. Blanvillain, H. Lu, A. C. Gossard, and D. J. Reilly, Frequency multiplexing for readout of spin qubits, *Appl. Phys. Lett.* **104**, 103108 (2014).
- [20] P. Harvey-Collard, N. T. Jacobson, C. Bureau-Oxton, R. M. Jock, V. Srinivasa, A. M. Mounce, D. R. Ward, J. M. Anderson, R. P. Manginell, J. R. Wendt, T. Pluym, M. P. Lilly, D. R. Lushman, M. Pioro-Ladrière, and M. S. Carroll, Spin-orbit Interactions for Singlet-Triplet Qubits in Silicon, *Phys. Rev. Lett.* **122**, 217702 (2019).
- [21] D. Jirovec, A. Hofmann, A. Ballabio, P. M. Mutter, G. Tavani, M. Botifoll, A. Crippa, J. Kukucka, O. Sagi, F. Martins *et al.*, A singlet-triplet hole spin qubit in planar Ge, *Nat. Mater.* **20**, 1106 (2021).
- [22] J. J. Pla, K. Y. Tan, J. P. Dehollain, W. H. Lim, J. J. L. Morton, F. A. Zwanenburg, D. N. Jamieson, A. S. Dzurak, and A. Morello, High-fidelity readout and control of a nuclear spin qubit in silicon, *Nature (London)* **496**, 334 (2013).
- [23] K. Ono, D. G. Austing, Y. Tokura, and S. Tarucha, Current rectification by Pauli exclusion in a weakly coupled double quantum dot system, *Science* **297**, 1313 (2002).
- [24] A. C. Johnson, J. R. Petta, C. M. Marcus, M. P. Hanson, and A. C. Gossard, Singlet-triplet spin blockade and charge sensing in a few-electron double quantum dot, *Phys. Rev. B* **72**, 165308 (2005).
- [25] J. M. Elzerman, R. Hanson, L. H. Willems van Beveren, B. Witkamp, L. M. K. Vandersypen, and L. P. Kouwenhoven, Single-shot read-out of an individual electron spin in a quantum dot, *Nature (London)* **430**, 431 (2004).
- [26] T. Meunier, K.-J. Tielrooij, I. T. Vink, F. H. L. Koppens, H. P. Tranitz, W. Wegscheider, L. P. Kouwenhoven, and L. M. K.

- Vandersypen, High fidelity measurement of singlet-triplet state in a quantum dot, *Phys. Status Solidi B* **243**, 3855 (2006).
- [27] S. A. Studenikin, J. Thorgrimson, G. C. Aers, A. Kam, P. Zawadzki, Z. R. Wasilewski, A. Bogan, and A. S. Sachrajda, Enhanced charge detection of spin qubit readout via an intermediate state, *Appl. Phys. Lett.* **101**, 233101 (2012).
- [28] M. A. Broome, T. F. Watson, D. Keith, S. K. Gorman, M. G. House, J. G. Keizer, S. J. Hile, W. Baker, and M. Y. Simmons, High-Fidelity Single-Shot Singlet-Triplet Readout of Precision-Placed Donors in Silicon, *Phys. Rev. Lett.* **119**, 046802 (2017).
- [29] M. A. Fogarty, K. W. Chan, B. Hensen, W. Huang, T. Tanttu, C. H. Yang, A. Laucht, M. Veldhorst, F. E. Hudson, K. M. Itoh *et al.*, Integrated silicon qubit platform with single-spin addressability, exchange control and single-shot singlet-triplet readout, *Nat. Commun.* **9**, 4370 (2018).
- [30] P. Harvey-Collard, B. D'Anjou, M. Rudolph, N. T. Jacobson, J. Dominguez, G. A. Ten Eyck, J. R. Wendt, T. Pluym, M. P. Lilly, W. A. Coish, M. Pioro-Ladrière, and M. S. Carroll, High-Fidelity Single-Shot Readout for a Spin Qubit via an Enhanced Latching Mechanism, *Phys. Rev. X* **8**, 021046 (2018).
- [31] L. A. Orona, J. M. Nichol, S. P. Harvey, C. G. L. Böttcher, S. Fallahi, G. C. Gardner, M. J. Manfra, and A. Yacoby, Readout of singlet-triplet qubits at large magnetic field gradients, *Phys. Rev. B* **98**, 125404 (2018).
- [32] W. Jang, J. Kim, M.-K. Cho, H. Chung, S. Park, J. Eom, V. Umansky, Y. Chung, and D. Kim, Robust energy-selective tunneling readout of singlet-triplet qubits under large magnetic field gradient, *npj Quantum Inf.* **6**, 64 (2020).
- [33] A. E. Seedhouse, T. Tanttu, R. C. C. Leon, R. Zhao, K. Y. Tan, B. Hensen, F. E. Hudson, K. M. Itoh, J. Yoneda, C. H. Yang, A. Morello, A. Laucht, S. N. Coppersmith, A. Saraiva, and A. S. Dzurak, Pauli blockade in silicon quantum dots with spin-orbit control, *PRX Quantum* **2**, 010303 (2021).
- [34] D. Keith, S. K. Gorman, L. Kranz, Y. He, J. G. Keizer, M. A. Broome, and M. Y. Simmons, Benchmarking high fidelity single-shot readout of semiconductor qubits, *New J. Phys.* **21**, 063011 (2019).
- [35] S. J. Hile, L. Fricke, M. G. House, E. Peretz, C. Y. Chen, Y. Wang, M. Broome, S. K. Gorman, J. G. Keizer, R. Rahman, and M. Y. Simmons, Addressable electron spin resonance using donors and donor molecules in silicon, *Sci. Adv.* **4**, eaaq1459 (2018).
- [36] Y. He, S. K. Gorman, D. Keith, L. Kranz, J. G. Keizer, and M. Y. Simmons, A two-qubit gate between phosphorus donor electrons in silicon, *Nature (London)* **571**, 371 (2019).
- [37] A. Abragam and M. Goldman, Principles of dynamic nuclear polarisation, *Rep. Prog. Phys.* **41**, 395 (1978).
- [38] S. Simmons, R. M. Brown, H. Riemann, N. V. Abrosimov, P. Becker, H.-J. Pohl, M. L. W. Thewalt, K. M. Itoh, and J. J. L. Morton, Entanglement in a solid-state spin ensemble, *Nature (London)* **470**, 69 (2011).
- [39] A. Morello, J. J. Pla, F. A. Zwanenburg, K. W. Chan, K. Y. Tan, H. Huebl, M. Möttönen, C. D. Nugroho, C. Yang, J. A. van Donkelaar *et al.*, Single-shot readout of an electron spin in silicon, *Nature (London)* **467**, 687 (2010).
- [40] Y.-L. Hsueh, H. Büch, Y. Tan, Y. Wang, L. C. L. Hollenberg, G. Klimeck, M. Y. Simmons, and R. Rahman, Spin-Lattice Relaxation Times of Single Donors and Donor Clusters in Silicon, *Phys. Rev. Lett.* **113**, 246406 (2014).
- [41] T. Fujisawa, T. H. Oosterkamp, W. G. van der Wiel, B. W. Broer, R. Aguado, S. Tarucha, and L. P. Kouwenhoven, Spontaneous emission spectrum in double quantum dot devices, *Science* **282**, 932 (1998).
- [42] Y. Wang, C.-Y. Chen, G. Klimeck, M. Y. Simmons, and R. Rahman, Characterizing Si:P quantum dot qubits with spin resonance techniques, *Sci. Rep.* **6**, 31830 (2016).
- [43] G. Klimeck, F. Oyafuso, T. B. Boykin, R. C. Bowen, and P. von Allmen, Development of a nanoelectronic 3-D (NEMO 3-D) simulator for multimillion atom simulations and its application to alloyed quantum dots, *Comput. Model. Eng. Sci.* **3**, 601 (2002).
- [44] G. Klimeck, S. S. Ahmed, Hansang Bae, N. Khariche, S. Clark, B. Haley, Sunhee Lee, M. Naumov, Hoon Ryu, F. Saied *et al.*, Atomistic simulation of realistically sized nanodevices using nemo 3-D—Part I: Models and benchmarks, *IEEE Trans. Electron Devices* **54**, 2079 (2007).
- [45] M. Simmons and J. Keizer, Method for selective incorporation of dopant atoms in a semiconductive surface, United States Patent US 11227768 B2 (2022).
- [46] J. A. Ivie, Q. Campbell, J. C. Koepke, M. I. Brickson, P. A. Schultz, R. P. Muller, A. M. Mounce, D. R. Ward, M. S. Carroll, E. Bussmann, A. D. Baczewski, and S. Misra, Impact of Incorporation Kinetics on Device Fabrication with Atomic Precision, *Phys. Rev. Appl.* **16**, 054037 (2021).
- [47] E. Bussmann, R. E. Butera, J. H. G. Owen, J. N. Randall, S. M. Rinaldi, A. D. Baczewski, and S. Misra, Atomic-precision advanced manufacturing for Si quantum computing, *MRS Bull.* **46**, 607 (2021).
- [48] J. Wyrick, X. Wang, P. Namboodiri, R. V. Kashid, F. Fei, J. Fox, and R. M. Silver, Enhanced atomic precision fabrication by adsorption of phosphine into engineered dangling bonds on H-Si using scanning tunneling microscopy and density functional theory, *arXiv:2112.12200*.
- [49] K. Wang, C. Payette, Y. Dovzhenko, P. W. Deelman, and J. R. Petta, Charge Relaxation in a Single-Electron Si/SiGe Double Quantum Dot, *Phys. Rev. Lett.* **111**, 046801 (2013).
- [50] R. M. Jock, N. T. Jacobson, P. Harvey-Collard, A. M. Mounce, V. Srinivasa, D. R. Ward, J. Anderson, R. Manginell, J. R. Wendt, M. Rudolph *et al.*, A silicon metal-oxide-semiconductor electron spin-orbit qubit, *Nat. Commun.* **9**, 1768 (2018).
- [51] M. Veldhorst, J. C. C. Hwang, C. H. Yang, A. W. Leenstra, B. de Ronde, J. P. Dehollain, J. T. Muhonen, F. E. Hudson, K. M. Itoh, A. Morello, and A. S. Dzurak, An addressable quantum dot qubit with fault-tolerant control-fidelity, *Nat. Nanotechnol.* **9**, 981 (2014).
- [52] R. Rahman, S. H. Park, T. B. Boykin, G. Klimeck, S. Rogge, and L. C. L. Hollenberg, Gate-induced g -factor control and dimensional transition for donors in multivalley semiconductors, *Phys. Rev. B* **80**, 155301 (2009).